Jurnal Kejuruteraan 38(7) 2026: 3495-3503
https://doi.org/10.17576/jkukm-2026-38(7)-27

Powder Injection Molding of Cu–Al–Ni Shape Memory Alloy Components: Feedstock Rheology and Sintering Response

Kambiz Rashidi[a,b], Abu Bakar Sulong[a,b*], Norhamidi Muhamad[a,b], Farhana Mohd Foudzi[a,b], Abdolali Fayyaz[c,d] & Al Basir[e]

[a]*Advanced Manufacturing Research Group, Universiti Kebangsaan Malaysia,*

43600 Bangi, Selangor, Malaysia

[b]*Department of Mechanical and Manufacturing Engineering, Faculty of Engineering and Built Environment,*

Universiti Kebangsaan Malaysia, 43600 Bangi, Selangor, Malaysia

[c]*Department of Materials Engineering, Science and Research Branch,*

Islamic Azad University, Tehran, Iran

[d]*Department of Advanced Materials & Processing, Research and Development of Engineering Materials Research Centre,*

Science and Research Branch, Islamic Azad University, Tehran, Iran

[e]*Interdisciplinary Research Center for Advanced Materials, King Fahd University of Petroleum and Minerals,*

Dhahran 31261, Saudi Arabia

[*]*Corresponding author: abubakar@ukm.edu.my*

Received 8 March 2026, Received in revised form 6 July 2026
Accepted 6 August 2026, Available online 30 October 2026

ABSTRACT

Cu–Al–Ni shape memory alloys (SMAs) are promising candidates for engineering applications because of their thermal stability, damping capacity, and relatively low cost compared with Ni–Ti SMAs. Powder injection molding (PIM) is a potential route for producing small and geometrically complex Cu–Al–Ni components; however, its success depends strongly on feedstock rheology, defect-controlled debinding, and suitable sintering response. In this study, 84Cu–12Al–4Ni (wt.%) SMA components were fabricated by PIM using a binder system composed of 65 wt.% paraffin wax, 30 wt.% high-density polyethylene, and 5 wt.% stearic acid. Feedstocks containing 64, 66, and 68 vol.% powder were prepared and rheologically evaluated. The 64 vol.% feedstock showed the most suitable rheological behavior, with favorable flow behavior index, flow activation energy, and general mobility index values. Defect-free green parts were produced by injection molding and subsequently subjected to solvent debinding in n-heptane at 60 ° C for 8 h, followed by thermal debinding at 500 °C for 75 min under Ar. Sintering at 1000 °C for 2.5 h promoted particle bonding and partial consolidation of the Cu–Al–Ni component. FESEM/EDS observations showed elemental interdiffusion together with carbon-rich regions, indicating that further debinding–sintering optimization is required. XRD analysis of the as-sintered component revealed α-Cu/Cu-rich and β/β_1-related phases, suggesting phase development after sintering and furnace cooling.

Keywords: Shape memory alloys; powder injection molding; sintering; characterization

INTRODUCTION

Shape memory alloys (SMAs) are a class of smart materials that can recover their original shape after deformation (Qader et al. 2019). This unique property arises from two different mechanisms, namely the shape memory effect (SME) and superelasticity (SE). Both phenomena are caused by a reversible solid-state martensitic phase transformation, whereby austenite (parent phase) is transformed into martensite and vice versa (Rashidi et al. 2024). In SMAs, austenite-martensite and martensite-austenite phase transformations occur during deformation and shape restoration, respectively. To achieve SME, the deformed SMAs should be heated above a certain temperature. However, during SE, both deformation and

shape recovery take place at a constant temperature (Kumar & Lagoudas 2008). Such unique properties of SMAs have enabled them to be used in many different industries such as aerospace (Bil et al. 2013), automotive (Jani et al. 2014) and robotics (Copaci et al. 2020). Among the various SMA systems, Ni–Ti alloys have achieved the highest level of commercial maturity, primarily owing to their excellent strain recovery capability relative to other major SMA categories (Alaneme & Okotete 2016). These alloys are also known for their desirable thermo-electrical properties and enhanced resistance to corrosion (Dawood & Abid Ali 2022). Despite these advantages, their widespread implementation in practical applications is still constrained by the relatively high cost associated with the alloying elements and processing routes (Alaneme et al. 2021; Muntasir Billah et al. 2022). In this regard, Cu-based SMAs have been proposed as promising alternatives to Ni–Ti systems because of their relatively low cost, large superelastic response, narrow thermal hysteresis, and high damping capacity (Dasgupta 2014; López et al. 2015; Saud et al. 2013). These alloys are commonly classified into Cu–Zn, Cu–Al, and Cu–Sn systems; however, challenges such as martensite stabilization and limited workability have encouraged the incorporation of ternary alloying elements to improve their functional performance (Dasgupta 2014). Among the widely investigated ternary Cu-based SMAs, including Cu–Zn–Al, Cu–Al–Mn, and Cu–Al–Ni, the Cu–Al–Ni system has attracted particular attention due to its high thermal stability up to approximately 200 °C, satisfactory damping behavior, and considerable recoverable nonlinear superelastic strain of about 18% (Saud et al. 2015; Suresh & Ramamurty 2008).

Various methods such as casting (Chang 2011), spray deposition (Agrawal & Vajpai 2020) and conventional powder metallurgy (Li et al. 2006) have been employed to produce SMAs. Nevertheless, these processing routes are often associated with several challenges when applied to Cu-based SMAs. In cast products, coarse-grained microstructures are commonly formed, which can increase brittleness and promote intergranular fracture. Therefore, cast polycrystalline Cu-based SMAs frequently require additional thermomechanical treatments or single-crystal processing to improve ductility (Abolhasani et al. 2023; Mazzer et al. 2022). Precise compositional control is also critical during casting, since even slight deviations from the desired stoichiometry may adversely affect the shape memory response (Mazzer et al. 2022). Similarly, conventional powder metallurgy may face limitations such as the requirement for high compaction pressure or sintering additives to obtain high densification, together with restricted capability for producing near-net-shaped components (Jean et al. 1991; Parvizi et al. 2021).

In this context, powder injection molding (PIM) offers a promising route for producing small and complex metallic components with good dimensional control, cost-effectiveness, and near-net-shape capability. The process generally consists of feedstock preparation, injection molding, debinding, and sintering (Basir et al. 2021). In this route, feedstock design is critical because powder loading, binder composition, viscosity, and shear-thinning behavior determine the moldability of the material and the quality of the injected green parts (Hausnerova 2010). After injection molding, controlled debinding is also essential because incomplete binder removal or defect formation during this stage may affect subsequent sintering through residual binder-derived contamination, nonuniform porosity, cracking, or restricted diffusion paths (Enneti et al. 2012). For Cu–Al–Ni components produced by PIM, sintering is particularly important because it must promote particle bonding, densification, and elemental interdiffusion while retaining the dimensional integrity of the component (Agrawal & Dube 2018). Therefore, successful fabrication of Cu–Al–Ni SMA components by PIM requires suitable feedstock rheology, defect-free shaping, controlled debinding, and appropriate sintering conditions. To the best of the authors' knowledge, the fabrication of Cu–Al–Ni SMA components through the PIM route has not yet been systematically reported, particularly with respect to the relationship between feedstock rheology, debinding integrity, and sintering response. Therefore, this study aims to investigate the feasibility of producing 84Cu–12Al–4Ni (wt.%) SMA components by PIM, with emphasis on identifying a suitable feedstock composition, producing defect-free green and debound parts, and evaluating the sintering response through microstructural, elemental, and phase analyses.

METHODOLOGY

A homogeneous 84Cu–12Al–4Ni (wt.%) powder mixture was prepared using gas-atomized elemental Cu, Al, and Ni powders. The critical powder volume concentration (CPVC) of the powder mixture was determined using the oil absorption method with a twin-screw blade Brabender® W50 EHT mixer. In this method, oleic acid was progressively added to the powder mixture while the variation in mixing torque was monitored. The torque reached its maximum value after the addition of 12 mL of oleic acid, as shown in Figure 1.

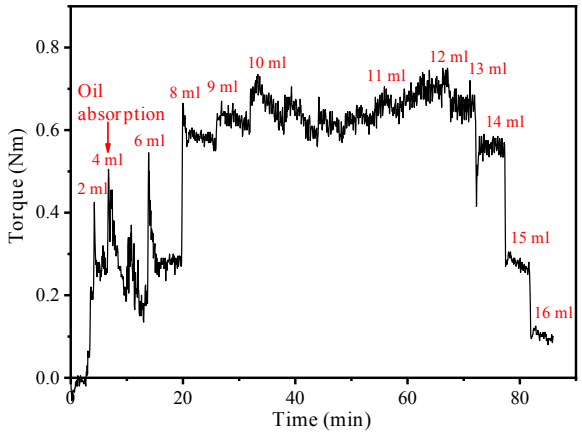


FIGURE 1. Variations of the mixing torque by adding oleic acid as a function of time

Based on this maximum volume of oleic acid, the critical powder volume concentration (CPVC) was calculated using Equation (1) and was found to be 69.61 vol.%.

$$CPVC\ (\%) = \frac{V_P}{V_P + V_O} \times 100 \quad (1)$$

where V_P is the volume of powder and V_o is the volume of oil.

Feedstocks containing 64, 66, and 68 vol.% powder were prepared by mixing the Cu–Al–Ni powder mixture with a three-component binder system. The binder system consisted of 65 wt.% paraffin wax (PW), 30 wt.% high-density polyethylene (HDPE), and 5 wt.% stearic acid (SA). This binder composition was selected with reference to previous studies on copper-based PIM feedstocks, in which wax-based binder systems containing PW, HDPE, and SA were shown to provide a suitable balance between flowability, green strength, and powder–binder compatibility (Ahmad et al. 2012; Moballegh et al. 2005). In the binder system, PW acted as the primary flow agent, HDPE served as the backbone polymer to maintain shape retention during debinding, and SA functioned as a surfactant to improve powder–binder interaction. The powder loadings were selected below the CPVC value to provide sufficient binder for moldability while maintaining high powder content for subsequent densification. Mixing was performed using the Brabender® W50 EHT mixer at 160 °C and 25 rpm for 45 min. During mixing, the powder mixture and binder constituents were gradually introduced into the mixing chamber until a homogeneous dough-like feedstock was obtained.

The rheological properties of the prepared feedstocks were evaluated using a Shimadzu® CFT 500EX capillary rheometer equipped with a die of 1 mm diameter and 10 mm length. The tests were performed at 145, 160, 175, and 190 °C under applied loads of 15, 35, 55, and 75 N. These measurements were used to determine the viscosity variation with shear rate and temperature, as well as the flow behavior index, flow activation energy, and general mobility index of the feedstocks. Each test was repeated three times to improve the reliability of the results.

Based on the rheological evaluation, the selected feedstock was used for injection molding. Green parts were produced using a DSM Xplore IM12 semi-automatic injection molding machine. The injection pressure was 10 bar, while the mold and melt temperatures were set at 140 °C and 165 °C, respectively. The injected green parts were visually inspected to identify possible molding defects before debinding.

The green parts were solvent debound in n-heptane at 60 °C for 8 h to remove the soluble binder constituents, mainly paraffin wax and stearic acid. The solvent-debound parts were then subjected to thermogravimetric analysis (TGA; NETZSCH STA 449F3) to evaluate the removal of the soluble binder fraction. Subsequently, thermal debinding was conducted at 500 °C for 75 min in a quartz tube furnace (TF-1200-30-35) under an Ar atmosphere. After visual inspection of the thermally debound parts for possible defects, the samples were subjected to a separate sintering cycle using the same quartz tube furnace.

Sintering was performed under an Ar atmosphere by heating the thermally debound samples at 2 °C/min to 1000 °C and holding for 2.5 h. After sintering, the samples were cooled to room temperature at 2 °C/min under the same atmosphere, visually inspected, sectioned, and prepared for microstructural observation. The microstructure and elemental distribution of the sintered samples were examined using field emission scanning electron microscopy equipped with energy-dispersive X-ray spectroscopy (FESEM/EDS, Zeiss Merlin Compact). The FESEM/EDS observations were used to evaluate particle bonding, residual porosity, elemental distribution, and the presence of carbon-rich or chemically nonuniform regions after sintering. The phase constitution of the as-sintered sample was further examined by X-ray diffraction (XRD) using a Bruker D8 diffractometer with Cu Kα radiation over a 2θ range of 20–100°. The sample was analyzed in the as-sintered condition without surface polishing, and the obtained XRD pattern was used to evaluate phase development after sintering and furnace cooling.

RESULTS AND DISCUSSION

RHEOLOGICAL TESTS

A suitable PIM feedstock should have low viscosity during injection, shear-thinning behavior, and good homogeneity to avoid powder–binder separation. When powder loading approaches the CPVC, particle spacing decreases and

friction increases, leading to higher viscosity and lower flow stability. However, too low powder loading may cause binder-rich regions, dimensional instability, and higher shrinkage. Figure 2 illustrates the rheological properties of the different feedstocks at various temperatures and shear rates. It can be observed that all feedstocks exhibited pseudoplastic behavior at all temperatures. This behavior occurs because the powder particles and polymer chains become aligned with the flow direction, reducing resistance to interparticle motion and producing shear-thinning behavior (Hausnerova 2010). Increasing the temperature decreased the viscosity of the feedstocks at a constant shear rate. This trend can be attributed to higher thermal expansion coefficient of the binder system compared to the powder mixture, resulting in raising the inter-particle distance and declining the viscosity (Islam et al. 2018).

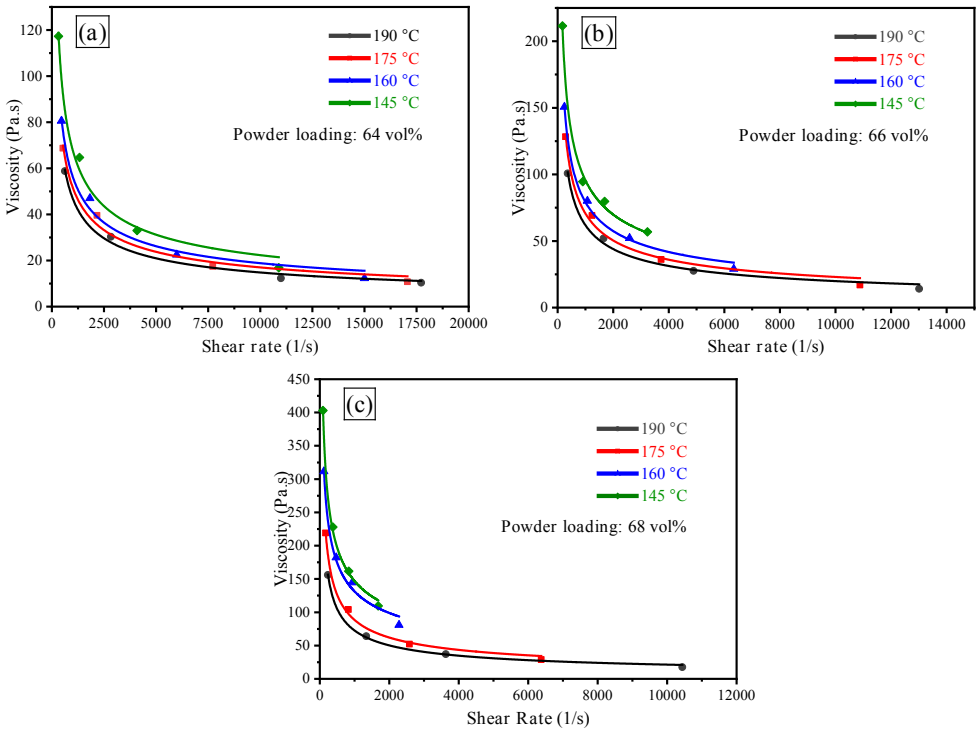


FIGURE 2. Rheological properties of the feedstocks at different temperatures

However, some factors should be taken into account to identify which pseudoplastic feedstock is more suitable for PIM. First, decreasing trend of viscosity of PIM feedstocks should exhibit low dependency on the rising shear rate. This is because intense viscosity reduction as the shear rate increases causes many injection defects like jetting and powder-binder separation (Islam et al. 2018). This factor is recognized by flow behavior index (n), which rises as the n values decline. Table 1 summarizes the n values of the different feedstocks at different temperatures. So, based on this data, it can be deduced that the 68 vol.% and 64 vol.% feedstocks are more suitable to be injected at lower temperatures (145 °C and 160 °C) and higher temperatures (175 °C and 190 °C), respectively. Also, viscosity of PIM feedstocks should have the minimized dependency to the variations of temperature. Intense viscosity changes due to temperature fluctuations can cause some defects in green parts such as stress concentration and cracks (Huang et al. 2003). Feedstock flow activation energy (E) represents the intensity of viscosity changes as the temperature fluctuates. Feedstocks with higher E exhibit increased viscosity dependency to the temperature variations. The E values E values were calculated at a constant shear rate of 1000 s^{-1} using the Arrhenius type equation as below:

$$\eta = \eta_0 \exp\left(\frac{E}{RT}\right) \quad (2)$$

where η_0 is a pre-exponential factor, R is the gas constant, and T is the absolute temperature.

The 64, 66 and 68 vol.% feedstocks possessed the E values of 12.63, 14.95 and 26.09 kJ/mol, respectively. Thus, the 64 vol.% feedstock is more desirable for PIM. The more important factor considering the dependency of viscosity to the variations of both shear rate and temperature simultaneously is general mobility index (α). Higher α values are associated with improved rheological properties

and better moldability of PIM feedstocks (Machaka et al. 2018). Therefore, based on the Table 1, the 64 vol.% feedstock, having the highest α values at all the temperatures, is more suitable for injection.

TABLE 1. Rheological indexes of the feedstocks

	Flow behavior index (n)				General mobility index (α)			
Powder loading	145 °C	160 °C	175 °C	190 °C	145 °C	160 °C	175 °C	190 °C
64 vol.%	0.51721	0.52406	0.51756	0.49901	4.6804	5.554	6.1445	7.0227
66 vol.%	0.54776	0.53845	0.51285	0.50726	2.6303	3.2413	3.8325	4.4262
68 vol.%	0.57664	0.5921	0.48811	0.46896	0.91797	0.9899	1.8436	2.3296

SOLVENT DEBINDING

Based on the rheological analysis results, defect-free green parts were produced using the 64 vol.% feedstock by the previously mentioned injection parameters. Then, the samples were subjected to solvent debinding. Figure 3 depicts a comparison between the TGA graphs of the green and solvent debound parts. These graphs reveal that the peak corresponding to the presence of paraffin wax and stearic acid was removed after solvent debinding. Figure 4 shows the solvent debound part and the corresponding FESEM micrograph from its surface. It can be observed that the sample retained its shape without visible cracking or distortion. Additionally, it can be seen that micro-pores formed on the surface of the sample, which can be attributed to the removal of paraffin wax and stearic acid. The extraction of these soluble binder constituents generated micropores that could provide diffusion pathways for the subsequent thermal removal of the HDPE backbone polymer. Therefore, it can be concluded that paraffin wax and stearic acid were successfully removed from the samples while no solvent debinding defects were observed.

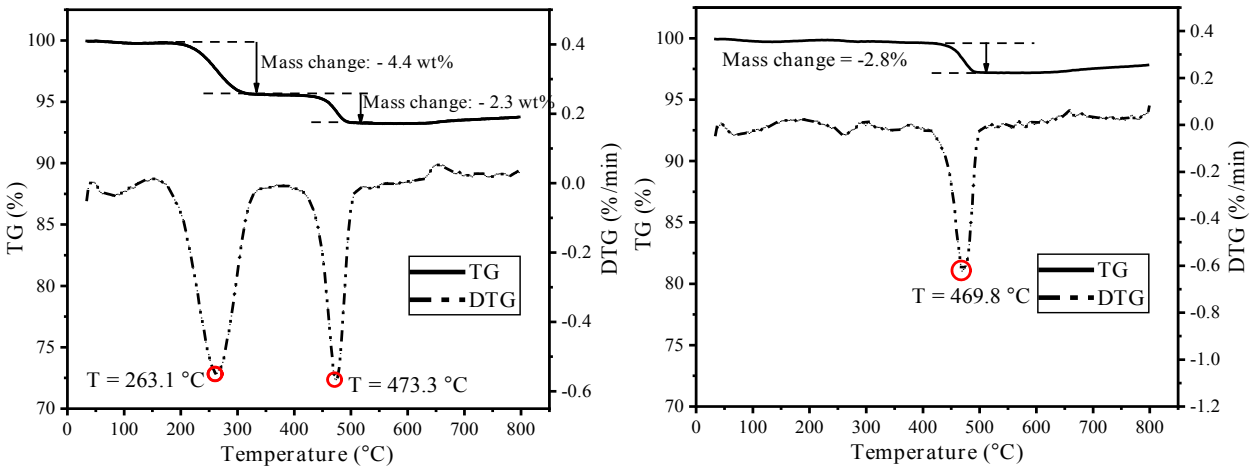


FIGURE 3. TGA results of (a) green part and (b) solvent debound part

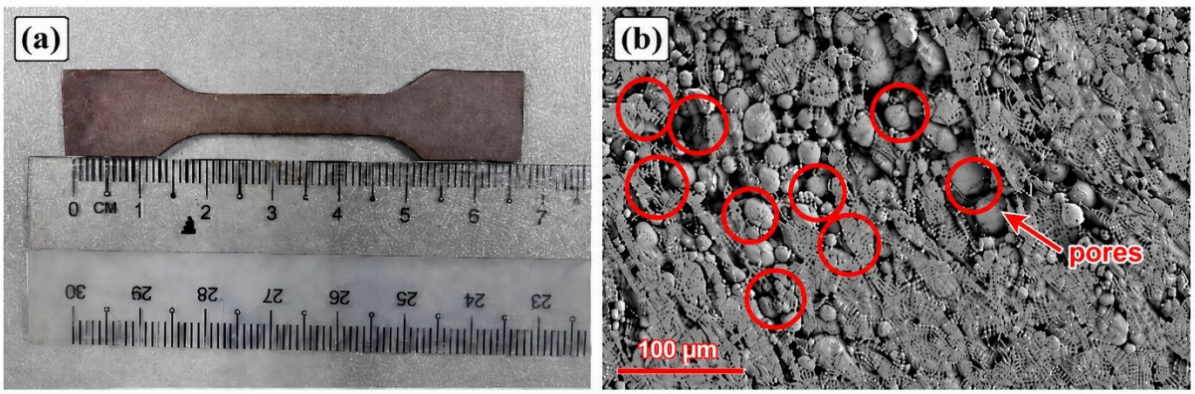


FIGURE 4. (a) Solvent-debound part and (b) micropores formed on the sample surface

THERMAL DEBINDING AND SINTERING

Figure 5 illustrates the thermal debinding cycle, as well as the cross-sectional FESEM micrograph of the thermally debound part. brown part after the thermal treatment. The thermal debinding cycle was designed as a staged heating process to allow gradual binder removal while preserving the integrity of the brown parts. Since the binder system consisted of paraffin wax, HDPE, and stearic acid, the lower-temperature holds were selected to assist the progressive removal of residual paraffin wax and stearic acid, whereas the higher-temperature holds at 420 and 500 °C were intended to promote the gradual decomposition of the HDPE backbone polymer. Slow heating rates of 30 and 20 °C/h were used during debinding to reduce rapid gas evolution and internal pressure, which may otherwise cause cracking, distortion, swelling, or collapse (Kan et al. 2021). The process was conducted under argon to limit oxidation of the Cu–Al–Ni powder compact during binder removal. The cross-sectional FESEM observation of the thermally debound sample revealed a porous structure consisting of exposed Cu–Al–Ni powder particles and interconnected void channels. The development of these open pore pathways suggests substantial removal of the binder system during the thermal debinding stage.

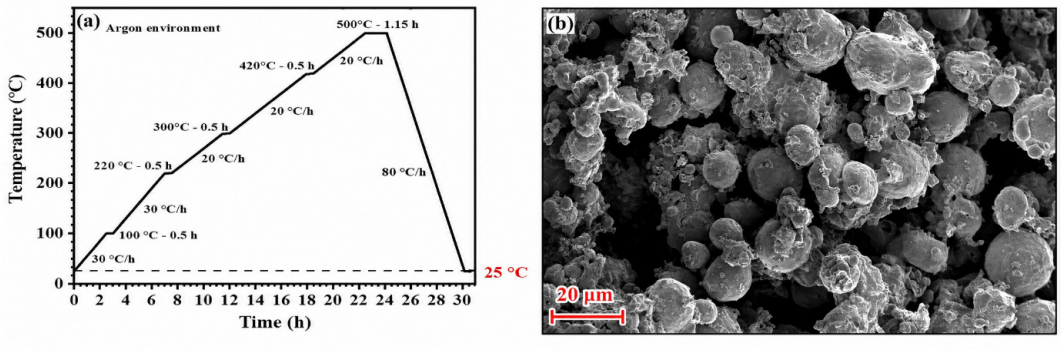


FIGURE 5. (a) Thermal debinding cycle and (b) cross-sectional FESEM of thermally debound part

Figure 6 shows the sintering cycle and the FESEM micrograph of the sintered component. The final sintering temperature of 1000 °C was selected to promote interparticle diffusion, neck growth, and alloy development in the Cu–Al–Ni compact, while the holding time was intended to provide sufficient particle bonding without excessive thermal exposure. As observed in the FESEM micrograph, several regions of the sample exhibited particle bonding and partial consolidation after sintering. Figure 7 shows the EDS elemental maps of the sintered component. The distribution of Cu, Al, and Ni indicates that interparticle diffusion and partial alloying occurred during sintering. However, chemically nonuniform regions and dark areas enriched in carbon were also observed. Since the carbon signal from EDS is qualitative, these regions may be associated with binder-derived carbonaceous residue or local chemical inhomogeneity, and further quantitative carbon analysis would be required for detailed confirmation. Therefore, the present sintering result should be interpreted as evidence of partial consolidation and phase development rather than complete homogenization or fully optimized sintering.

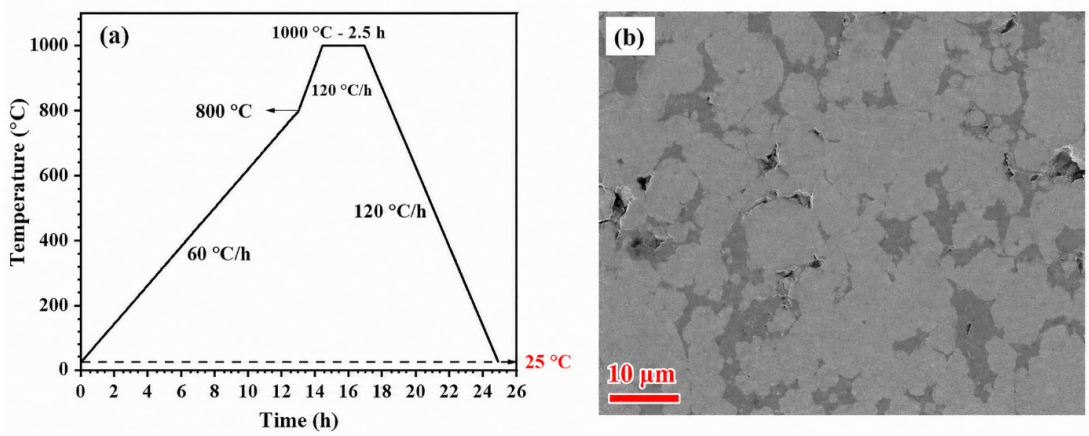


FIGURE 6. (a) Sintering thermal cycle and (b) FESEM micrograph of the sintered part

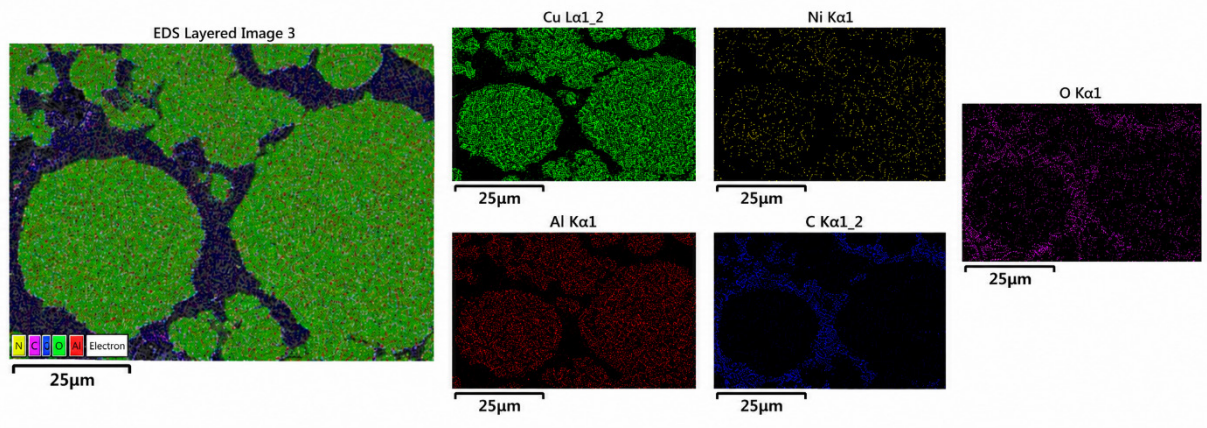


FIGURE 7. EDS map of the sintered part

PHASE ANALYSIS OF THE AS-SINTERED COMPONENT

Figure 8 shows the XRD pattern of the as-sintered Cu–Al–Ni component produced after thermal debinding at 500 °C for 75 min and sintering at 1000 °C for 2.5 h under an Ar atmosphere. The diffraction pattern shows several intense peaks at approximately 42.82°, 49.86°, 73.12°, 88.58°, and 93.64°, which can be assigned to the FCC α-Cu/Cu-rich phase. The presence of these peaks indicates that a Cu-rich equilibrium phase was formed or retained after sintering and furnace cooling. This is reasonable because the sample was furnace-cooled after sintering, which may promote the formation of equilibrium phases rather than preserving a fully high-temperature parent phase. In addition to the α-Cu/Cu-rich reflections, peaks observed at approximately 44.26°, 64.34°, 81.36°, and 97.64° may be associated with a β/β_1-related BCC parent phase. The appearance of these peaks suggests that sintering promoted alloying and phase development in the Cu–Al–Ni compact through interparticle diffusion. However, the coexistence of α-Cu/Cu-rich and β/β_1-related phases indicates that the as-sintered component did not form a fully single-phase β structure under the present sintering and cooling conditions.

Some weak reflections were also detected in the XRD pattern, which may be related to some unidentified minor reflections Overall, the XRD results support the FESEM/EDS observations by confirming that sintering promoted partial alloy formation and phase development in the Cu–Al–Ni component. The detection of β/β_1-related parent-phase reflections is an encouraging indication that a phase constituent relevant to subsequent martensitic transformation may be present in the as-sintered alloy. Although martensite was not observed in the as-sintered condition, the presence of the parent phase suggests that appropriate post-sintering thermal treatment, followed by rapid quenching from the β-phase region, may promote the formation of martensite and enable the development of shape memory behavior in the Cu–Al–Ni alloy (Agrawal & Dube 2018; Rashidi et al. 2024).

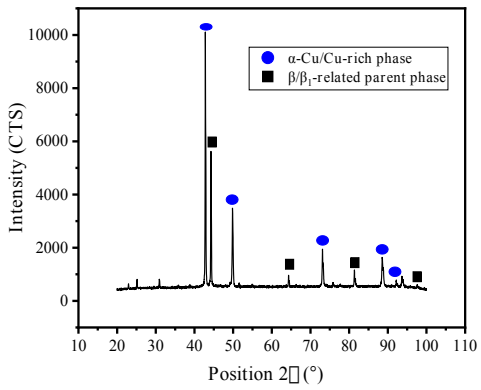


FIGURE 8. XRD pattern of the as-sintered Cu–Al–Ni component

CONCLUSION

In this study, the feasibility of producing 84Cu–12Al–4Ni (wt.%) SMA components by powder injection molding was investigated by focusing on feedstock rheology, debinding integrity, sintering response, and phase development in the as-sintered condition. The main conclusions are as follows:

1. All feedstocks containing 64, 66, and 68 vol.% powder exhibited pseudoplastic behavior, which is desirable for PIM processing. Among them, the 64 vol.% feedstock showed the most suitable rheological performance because of its favorable flow behavior index, lower flow activation energy, and higher general mobility index.
2. Defect-free green parts were successfully produced using the selected feedstock and

injection parameters. Solvent debinding in n-heptane at 60 °C for 8 h removed the soluble binder constituents and formed surface micropores, while the subsequent thermal debinding cycle was highly successful in removing the remaining polymeric binder.

3. Sintering at 1000 °C for 2.5 h under Ar promoted particle bonding, partial consolidation, and elemental interdiffusion in the Cu–Al–Ni component. However, FESEM/EDS analysis also revealed carbon-rich and chemically nonuniform regions, indicating that further optimization of the debinding and sintering conditions is required.
4. XRD analysis of the as-sintered component revealed reflections corresponding to α-Cu/Cu-rich and β/β□-related phases. The coexistence of these phases indicates that sintering and furnace cooling led to phase development, but not to a fully single-phase β structure. The β/β□-related reflections are relevant to future post-sintering heat treatment and quenching studies aimed at promoting martensitic transformation and shape memory behavior.

ACKNOWLEDGEMENT

The authors would like to thank the Ministry of Higher Education Malaysia (MOHE) and Universiti Kebangsaan Malaysia (UKM) for the financial support that they provided via the Fundamental Research Grant FRGS/1/2021/TK0/UKM/01/2.

DECLARATION OF COMPETING INTEREST

None.

REFERENCES

Abolhasani, D., Kwon, H.-N., Park, Y.-H. & Moon, Y.-H. 2023. Enhancing the mechanical properties of Cu–Al–Ni shape memory alloys locally reinforced by alumina through the powder bed fusion process. *Materials* 16: 3936.

Agrawal, A. & Dube, R.K. 2018. Methods of fabricating Cu-Al-Ni shape memory alloys. *Journal of Alloys and Compounds* 750: 235-247.

Agrawal, A. & Vajpai, S.K. 2020. Preparation of Cu–Al–Ni shape memory alloy strips by spray deposition-hot rolling route. *Materials Science and Technology* 36: 1337-1348.

Ahmad, F., Muhsan, A.S. & Raza, M.R. 2012. Rheological behavior of carbon nanotubes/copper feedstocks for metal injection molding. *Advanced Materials Research* 403: 5335-5340.

Alaneme, K.K., Anaele, J.U. & Okotete, E.A. 2021. Martensite aging phenomena in Cu-based alloys: Effects on structural transformation, mechanical and shape memory properties: A critical review. *Scientific African* 12.

Alaneme, K.K. & Okotete, E.A. 2016. Reconciling viability and cost-effective shape memory alloy options–A review of copper and iron-based shape memory metallic systems. *Engineering Science and Technology, an International Journal* 19: 1582-1592.

Basir, A., Sulong, A.B., Jamadon, N.H., Muhamad, N. & Emeka, U.B. 2021. Process parameters used in macro/micro powder injection molding: an overview. *Metals and Materials International* 27: 2023-2045.

Bil, C., Massey, K. & Abdullah, E.J. 2013. Wing morphing control with shape memory alloy actuators. *Journal of Intelligent Material Systems and Structures* 24: 879-898.

Chang, S.H. 2011. Influence of chemical composition on the damping characteristics of Cu–Al–Ni shape memory alloys. *Materials Chemistry and Physics* 125: 358-363.

Copaci, D.-S., Blanco, D., Martin-Clemente, A. & Moreno, L. 2020. Flexible shape memory alloy actuators for soft robotics: Modelling and control. *International Journal of Advanced Robotic Systems* 17.

Dasgupta, R. 2014. A look into Cu-based shape memory alloys: Present scenario and future prospects. *Journal of Materials Research* 29: 1681-1698.

Dawood, N.M. & Abid Ali, A.R. 2022. Effect of aging on corrosion behavior of martensite phase in Cu-Al-Ni shape memory alloy. *Key Engineering Materials* 911: 96-102.

Enneti, R.K., Park, S.J., German, R.M. & Atre, S.V. 2012. Thermal debinding process in particulate materials processing. *Materials and Manufacturing Processes* 27: 103-118.

Hausnerova, B. 2010. Rheological characterization of powder injection molding compounds. *Polimery* 55: 3-11.

Huang, B., Liang, S. & Qu, X. 2003. The rheology of metal injection molding. *Journal of Materials Processing Technology* 137: 132-137.

Islam, S.T., Samanta, S.K., Roy, H., Lohar, A.K., Das, S. & Bandyopadhyay, A. 2018. Rheological behavior of 316L stainless steel feedstock for μ-MIM. *Materials Today: Proceedings* 5: 8152-8158.

Jani, J.M., Leary, M., Subic, A. & Gibson, M.A. 2014. A review of shape memory alloy research, applications and opportunities. *Materials & Design* (1980-2015) 56: 1078-1113.

Jean, R., Wu, T. & Leu, S. 1991. The effect of powder metallurgy on Cu-Al-Ni shape memory alloys. *Scripta Metallurgica et Materialia* 25: 883-888.

Kan, X., Yang, D., Zhao, Z. & Sun, J. 2021. 316L FFF binder development and debinding optimization. *Materials Research Express* 8: 116515.

Kumar, P. & Lagoudas, D. 2008. Introduction to shape memory alloys. In *Shape Memory Alloys: Modeling and Engineering Applications*, pp. 1-51. USA: Springer.

Li, Z., Pan, Z.Y., Tang, N., Jiang, Y.B., Liu, N., Fang, M. & Zheng, F. 2006. Cu–Al–Ni–Mn shape memory alloy processed by mechanical alloying and powder metallurgy. *Materials Science and Engineering*: A 417: 225-229.

López, G., López-Ferreño, I., Kilmametov, A., Breczewski, T., Straumal, B., Baretzky, B., Nó, M. & San Juan, J. 2015. Severe plastic deformation on powder metallurgy Cu–Al–Ni shape memory alloys. *Materials Today: Proceedings* 2: S747-S750.

Machaka, R., Ndlangamandla, P. & Seerane, M. 2018. Capillary rheological studies of 17-4 PH MIM feedstocks prepared using a custom CSIR binder system. *Powder Technology* 326: 37-43.

Mazzer, E.M., da Silva, M.R. & Gargarella, P. 2022. Revisiting Cu-based shape memory alloys: Recent developments and new perspectives. *Journal of Materials Research* 37: 162-182.

Moballegh, L., Morshedian, J. & Esfandeh, M. 2005. Copper injection molding using a thermoplastic binder based on paraffin wax. *Materials Letters* 59: 2832-2837.

Muntasir Billah, A.H.M., Rahman, J. & Zhang, Q. 2022. Shape memory alloys (SMAs) for resilient bridges: A state-of-the-art review. *Structures* 37: 514-527.

Parvizi, S., Hashemi, S.M., Asgarinia, F., Nematollahi, M. & Elahinia, M. 2021. Effective parameters on the final properties of NiTi-based alloys manufactured by powder metallurgy methods: A review. *Progress in Materials Science* 117: 100739.

Qader, I.N., Kök, M. & Dağdelen, F. 2019. Effect of heat treatment on thermodynamics parameters, crystal and microstructure of (Cu-Al-Ni-Hf) shape memory alloy. *Physica B: Condensed Matter* 553: 1-5.

Rashidi, K., Sulong, A.B., Muhamad, N., Fayyaz, A., Foudzi, F.M. & Basir, A. 2024. Martensitic transformation characteristics, mechanical properties and damping behavior of Cu–Al–Ni shape memory alloys: A review of their modifications and improvements. *Journal of Materials Research and Technology* 29: 2732-2749.

Saud, S.N., Hamzah, E., Abubakar, T. & Hosseinian, R. 2013. A review on influence of alloying elements on the microstructure and mechanical properties of Cu-Al-Ni shape memory alloys. *Jurnal Teknologi* 64: 51-56.

Saud, S.N., Hamzah, E., Abubakar, T., Ibrahim, M.K. & Bahador, A. 2015. Effect of a fourth alloying element on the microstructure and mechanical properties of Cu–Al–Ni shape memory alloys. *Journal of Materials Research* 30: 2258-2269.

Suresh, N. & Ramamurty, U. 2008. Aging response and its effect on the functional properties of Cu–Al–Ni shape memory alloys. *Journal of Alloys and Compounds* 449: 113-118.